An Improved Robust Model Predictive Speed Control With Inertia Identification for PMSM Drives in the Electrohydrostatic Actuator

Taoming Wang, *Student Member, IEEE*, Guangzhao Luo, *Senior Member, IEEE*, Zhe Chen, *Member, IEEE*, Wencong Tu, *Member, IEEE*, and Chunqiang Liu, *Member, IEEE*

***Abstract*—Electrohydrostatic actuator (EHA), composed of permanent-magnet motors, is an integrated local hydraulic actuation system and has been utilized as the flight surface actuation in all/more electrical aircraft. The motor drives of the EHA require a strong antidisturbance performance and robustness owing to the "variable speed/ variable load" conditions, which presents a challenge for the traditional field-oriented control. In this study, an improved robust model predictive speed control is put forward to enhance the load rejection performance and robustness. The characteristics of the aerodynamic load and the loads on the swash plate axial piston pump are first examined. Following the investigation of the discretization-related errors, the second-order modified discrete model based on the forward Euler (FE) and backward Euler (BE) methods both is presented. Based on the modified FE discrete model, a modified extended state observer (ESO) is presented to obtain a more accurate estimate of the disturbance during the transient state. Meanwhile, to lessen the effect of the mismatched inertia moment on the ESO, a modified moving horizon estimator based on the multiinstant BE discrete model is proposed . Finally, simulation and experiment results demonstrate the effectiveness, improved antidisturbance performance, and robustness by contrasting the proposed approach with the conventional model predictive speed control.**

***Index Terms*—Model predictive control (MPC), robust control, variable speed drives.**

I. Introduction

THE concept of power-by-wire (PbW) is introduced to the actuation system of flight surfaces in all/more electrical aircraft. By transferring electrical control signals to the actuation system, the flight surface can be controlled with efficiency and reliability. An electrohydrostatic actuator (EHA), composed of a permanent-magnet motor speed drive system and a self-contained hydraulic system, is one kind of PbW actuation. According to the control signal sent by the flight computer, the speed and steering of the motor drive system are adjusted to achieve the contraction and extension of the stroke rod. Fig. 1 shows the EHA system composition.

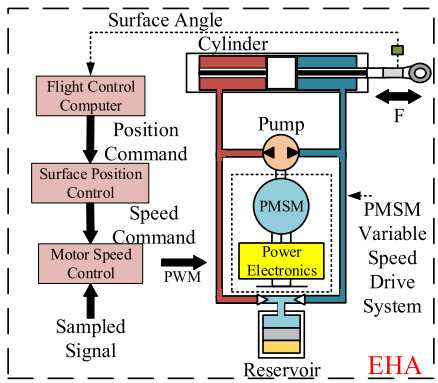

Fig. 1. Block diagram of the EHA system.

Through decades of development, the EHA has been employed in the flight surface control actuation system of modern commercial aircraft, e.g., the aileron of the B787 and A350 [1]. Compared with the centralized hydraulic actuation systems, the EHA has the advantages of higher reliability and lower weight due to the reduction of hydraulic pipes and valves. By employing the EHA, the reduced weights for the aircrafts A320, A340, and A380 are 100, 250, and 450 kg, respectively [2]. In the future, the solution for the EHA will be developed in the direction of high hydraulic pressure and high rotor speed to increase the power density.

The EHA works under variable load and variable speed conditions during the flight process. Considering the existence of aerodynamic load, the disturbance rejection performance of the EHA is essential. In addition, the swash plate angle of the EHA pump would be changed to adjust the displacement in real time, which cause a change in motor inertia load. Therefore, the

Manuscript received 10 January 2023; revised 25 June 2023; accepted 7 August 2023. Date of publication 14 August 2023; date of current version 22 September 2023. This work was supported in part by the National Natural Science Foundation of China under Grant 52177059, in part by the Gansu Provincial Science and Technology Plan under Grant 22ZD6GA027, in part by the Key Research and Development Plan of Shaanxi Province under Grant 2022GY-264, and in part by the Shaanxi Key Laboratory of Small and Special Electrical Machine and Drive Technology. Recommended for publication by Associate Editor H. Hofmann. *(Corresponding author: Guangzhao Luo.)*

Taoming Wang, Guangzhao Luo, and Zhe Chen are with the School of Automation, Northwestern Polytechnical University, Xi'an 710072, China (e-mail: wtm001@mail.nwpu.edu.cn; guangzhao.luo@nwpu.edu.cn; zhe.chen@nwpu.edu.cn).

Wencong Tu is with the Shaanxi Aero Electric Co. Ltd, Xi'an 710065, China (e-mail: wencongtu@mail.nwpu.edu.cn).

Chunqiang Liu is with the Hangzhou Institute of Technology, Xidian University, Hangzhou 311231, China (e-mail: liuchunqiang22@126.com).

Color versions of one or more figures in this article are available at https://doi.org/10.1109/TPEL.2023.3304657.

Digital Object Identifier 10.1109/TPEL.2023.3304657

motor drive system serves as the power transfer source of the EHA, it is essential to improve the antidisturbance performance and robustness of the variable speed motor drive system. Besides, the required high control performances are a challenge for the traditional field-oriented control adopted in the motor control loop in the EHA. In recent years, to improve the control performance, many enhanced control strategies have been explored for the motor drive system of the EHA, e.g., nonlinear proportional-integral-derivative (PID) [4], sliding-mode control [5], and fuzzy control [6]. However, experiments are required to obtain the optimal PID parameters for the highly nonlinear EHA plant model. Other complex control strategies would increase the computational burden of digital processors. Meanwhile, most of the control strategies do not compensate the internal and external disturbances.

Model predictive control (MPC) has been receiving abundant attention due to the advantages of sample, intuitive, and flexible integration of constraints [42]. The model-based control strategy with rolling optimization makes MPC output local optimal variables in every control cycle [7]. MPC can be divided into two types that include finite-control-set model predictive control (FCS-MPC) and continuous-control-set model predictive control (CCS-MPC) [8]. For the FCS-MPC, the multiobjectives cost function is used to evaluate all candidate voltage vectors. To achieve high dynamic speed tracking performance, model predictive direct speed control (MPDSC) based on FCS-MPC is proposed by integrating the outer and inner loops into one control loop [9], [10], [11]. Although the MPDSC has a cost function that can be set flexibly and demonstrates an improved dynamic behavior, but the numbers of weighting factors should be tuned to optimal values. Meanwhile, the stability and robustness of the control system need to be explored due to the limited margins of the single-loop structure.

CCS-MPC calculates and outputs continuous state quantities according to predefined optimization criteria, and has the characteristics of high dynamic performance. To realize that motor speed tracks reference quickly and smoothly, continuous-control-set model predictive speed control (CCS-MPSC) has been proposed [12]. CCS-MPSC, which has a cascade control structure, adopts a mechanical dynamic model as prediction model and calculates q-axis current reference based on the predetermined control law. Ahmed et al. [13] compare the dynamic experiment behavior of MPSC based on FCS and CCS, respectively. To improve the disturbance rejection performance, the ultralocal model is presented by combining uncertain and inaccuracy parameters into lump disturbances. The lump disturbances and state variables of CCS-MPSC can be identified by classical observers such as recursive least square (RLS), extended state observer (ESO), and sliding-mode control (SMC). In [14], flux linkage and speed variables are estimated by RLS and integral sliding-mode observer to improve the robustness of the control system. Besides, several novel CCS-MPSC based on improved SMC are explored, in which a new cost index is designed [15], [16], [17], [18]. Active disturbance rejection control (ADRC), proposed by *Han*, is implemented in motion control due to the advantages of rich theoretical basic and strong disturbance rejection performance. Many recent works have been presented based on ADRC and MPC. In [19], linear ESOs are applied in CCS-MPSC to improve the control performance. In [20] and [21], variable bandwidth ESO and control law based on the *fal* function are presented to CCS-MPSC. However, the impact of mismatched mechanical parameters has not been considered. In [22], a novel ESO with parameter identification is proposed to improve the accuracy of the prediction model. Unfortunately, the accuracy of the discrete model has not been analyzed, which has potential to be further improved.

In this article, to oscillate the impact of load torque and mismatched mechanical parameters, a novel robust CCS-MPSC with a modified discrete model is proposed. The contributions of this article are described as follows.

1) To improve the accuracy of the predictive model in transient state and steady state, the modified second-order forward Euler (FE) and backward Euler (BE) discrete models are presented. Comparing with classical discrete models, the discretization error can be reduced significantly.
2) Based on the modified second-order FE discretized mechanical dynamic equation, a modified ESO (MESO) is proposed to obtain a more precise estimated result. Meanwhile, a novel control law based on modified ESO is proposed to improve the transient-state and steady-state performance.
3) The impact of the mismatched moment of inertia on ESO is analyzed in the z-domain. To eliminate the impact, a modified moving horizon estimator (MMHE) with long horizon is presented based on the modified second-order BE discrete model. The estimated inertia moment is used to improve the antidisturbance and robust performance.
4) The magnitude characteristic of the proposed method affected by weighting factors is analyzed by the Bode integral theorem in the z-domain. Meanwhile, the calculation process of the basic weighting factors is presented. The proposed method is implemented in field-programmable gate array (FPGA), in which the parallel pipeline architecture is adopted to reduce the computational burden.

The rest of this article is organized as follows. Section II explores the attributes of EHA disturbances and the causes of perturbed inertia moment. Section III describes the investigation of the conventional CCS-MPSC based on ESO. Section IV proposes a novel robust CCS-MPSC based on MESO and MMHE. Section V proves the validity of the proposed robust CCS-MPSC by simulation and experiment. Finally, Section VI concludes this article.

II. Characteristics of External and Internal Disturbances

It is well known that external aerodynamic disturbances (e.g., gust and turbulence) and internal disturbances (e.g., friction and pump load) would generate a negative impact on the speed tracking performance of the EHA. Therefore, a study on upcoming loads is essential and is beneficial for designing an improved control method for the motor variable speed drive system of the EHA.

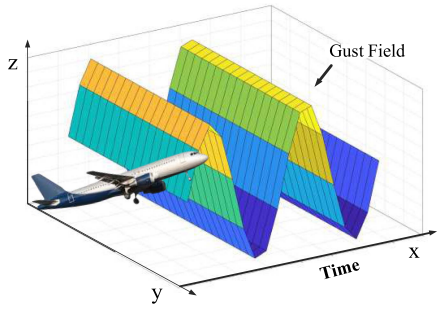

Fig. 2. Aircraft facing a spatially frozen turbulence field.

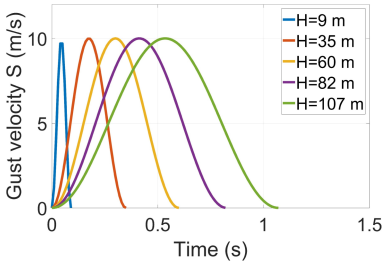

Fig. 3. Discrete gust at 200-m/s airspeed.

A. External Disturbances

The EHA in a cruise flying aircraft will be affected by external working environment disturbances that are mostly composed of the encountering gusts. Generally, gusts are assumed to be frozen in space. That means a gust will affect the flight surface with identical amplitude. The duration depends on the aircraft's forward velocity [23]. Fig. 2 shows the aircraft facing a gust field. According to the CS25 certification from the European Aviation Safety Agency and FAR25 (Federal Aviation Regulations, Part 25[2]), disturbances are classified into two categories: discrete gust (1-cos) and continuous turbulence.

The shape of one-minus-cosine (1-cos) gust is specified as

$$S = \frac{1}{2} S_0 \left(1 - \cos \frac{2\pi V}{2H} t\right), 0 \le t \le \frac{2H}{V} \tag{1}$$

where S is the gust velocity; S_0 is the maximum gust velocity; V means airspeed; and H is the gust gradient that varied between 9 and 107 m for the case of the commercial aircraft. Fig. 3 shows the 1-cos gusts at 200 m/s with 9∼107-m gradient. The 1-cos gusts are seen as the main load that need to be reduced for the wing load alleviation system [24]. Considering EHAs placing in the ailerons, the discrete 1-cos gusts can be seen the external loads.

The continuous turbulence is typically irregular, which can be idealized as a "stationary Gaussian random process" [25]. The Gaussian random process can be simplified as the combination of the infinite number of sinusoidal components with random amplitude and frequency. In that case, continuous turbulence is formed by the combination of multiple discrete gusts, whose frequencies are typically below 30 Hz [23].

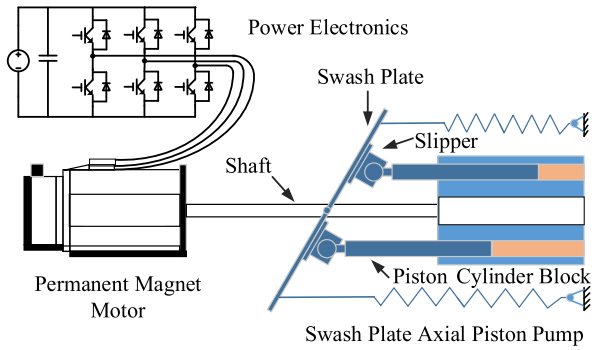

Fig. 4. Block diagram of motor drive axial piston pump.

B. Internal Disturbances

For the variable pump variable motor EHA (VPVM-EHA), a variable displacement swash plate axial piston pump is driven by a permanent-magnet motor to transfer mechanical energy due to high operating efficiencies (85%–95%) and pressure (42 MPa). Assuming the piston pump and hydraulic oil work in ideal condition without energy loss and with constant pressure, the pump load characteristics are explored as follows.

The axial piston pump is composed of machine components, including odd/even number of pistons, shaft, swash plate, cylinder, etc. Fig. 4 shows the pump configurations [26]. The input shaft load is calculated by summing all the forces exerted on the components. Thus, the average load $\bar{T}$ acting on the input shaft is expressed as

$$\bar{T} = \frac{N}{\pi} A_p \tan(\alpha) r P_d \left(1 - \frac{P_i}{P_d}\right) \tag{2}$$

where A_p means cross-sectional area of a single piston; α is the swash plate angle; r is the piston pitch radius; N is total number of pistons; P_d is the pump discharge pressure; and P_i is the pump intake pressure.

Ignoring the load ripples during the piston pass from the intake port to the discharge port (1.5% amplitude of loads), the average input shaft load is a constant load for a known configuration [27].

C. Perturbed Inertia Moment of the Motor Drive System in the EHA

Due to the requirement of high maneuver, the flight surface is controlled frequently in "high hydraulic pressure/ large pump displacement/ variable motor speed" conditions. To obtain the required pump displacement, the displacement can be changed by adjusting the angle of the swash plate. According to [28], the inertia forces vary with angle of the swash plate in a cosine trend. Meanwhile, increased pump speed would increase the inertia force and centrifugal moments. In that way, the inertia moment of the motor drive system is a coefficient that needs to be identified in real time to improve the accuracy of the motor mathematical model. Therefore, the robustness against the mismatched inertia moment of the motor drive system is essential to be improved. Table I summarizes the disturbances of the EHA.

TABLE I
DISTURBANCES OF THE EHA

Disturbances		Characteristics
External Disturbances	Discrete gust	(1)
	Continuous turbulence	Combination of multiple discrete gusts
Internal Disturbances	Pump load	(2)
	Perturbed inertial moment	Vary with angle of swash plate and pump speed

III. PRINCIPLE OF THE CONVENTIONAL CCS-MPSC BASED ON THE ESO

A. Mechanical Dynamic Model of the Surface-Mounted Permanent-Magnet Synchronous Motor (SPMSM)

Due to the high torque-to-current ratio and high efficiency, an SPMSM is widely utilized in the EHA [29]. The mechanical dynamic model of the SPMSM is expressed as

$$\begin{cases} \frac{d\omega_m}{dt} = \frac{1}{J}\left[T_e - B\omega_m - C\text{sign}\left(\omega_m\right) - T_L\right] \\ \frac{dT_L}{dt} = d,\ \frac{dJ}{dt} = 0,\ \frac{dB}{dt} = 0,\ \frac{dC}{dt} = 0 \end{cases} \tag{3}$$

where ω_m is the rotor angular velocity; J is the moment of inertia; B and C are the viscous and Coulomb friction torque coefficients, respectively; and T_L is load torque of the SPMSM. The derivations of the mechanical parameters J, B and C are assumed to be zero because of the low varying rate.

Due to the lack of rank, the multimechanical parameters in (3) cannot be identified at the same time, especially when $d\omega_m/dt = 0$ in steady state [30]. To address this problem, the ultralocal prediction model is presented by combining load torque and inaccuracy mechanical parameter loads to the lump load T_f, which is expressed as

$$\begin{cases} J\dfrac{d\omega_m}{dt} = T_e - T_f & \text{(4a)} \\ \dfrac{dT_f}{dt} = g & \text{(4b)} \end{cases}$$

where defining $\Delta B, \Delta J$, and ΔC as perturbed value and J_0, B_0, and C_0 as initial value, lump disturbance is defined as follows:

$$T_f = \left[\left(B_0+\Delta B\right)\omega_m + \left(C_0+\Delta C\right)\text{sign}\left(\omega_m\right) + T_L\right] + \Delta J\frac{d\omega_m}{dt}. \tag{5}$$

By adopting ultralocal model, the number of mechanical parameters is reduced. Based on (4), a conventional CCS-MPSC based on extended state observer (ESO) is presented.

B. Conventional CCS-MPSC Based on ESO

By using the FE method, the ESO taking ω_m and d ($d = -T_f/J$) as variables is designed as follows:

$$\begin{cases} e_\omega\ (k) = \hat{\omega}_m\ (k) - \omega_m\,(k) \\ \hat{\omega}_m\ (k+1) = \hat{\omega}_m\ (k) + T_s\left[\frac{1}{J}T_e\,(k) + \hat{d}\,(k)\right] - T_s\beta_1 e_\omega\,(k) \\ \hat{d}\ (k+1) = \hat{d}\ (k) - T_s\beta_2 e_\omega\,(k) \end{cases} \tag{6}$$

where $\beta_1 = 2\omega_0$ and $\beta_2 = \omega_0^2$ are gains of the ESO according to the analysis of stability [3]; ω_0 represents the bandwidth of the ESO; T_s is the sample period of the external loop; and $\hat{\omega}_m(k)$ and $\hat{d}(k)$ means the estimated rotor angle velocity and estimated load at k instant.

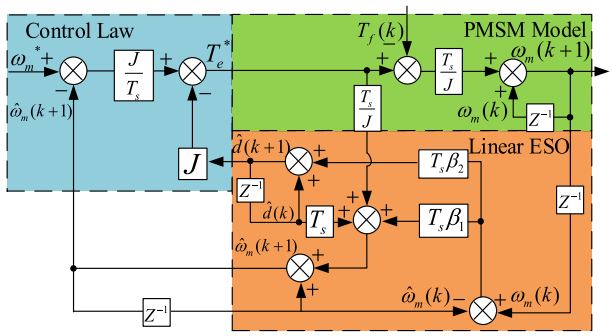

Fig. 5. Block diagram of the conventional CCS-MPSC.

The cost function is designed as follows:

$$J_c = \left[\omega_m^* - \hat{\omega}_m\left(k+1\right)\right]^2 \tag{7}$$

where ω_m^* represents the reference angle velocity. By solving $\partial J_c/\partial T_e(k) = 0$, the optimal control law is obtained, which is shown as follows:

$$T_e^{ref} = \frac{J[\omega_m^* - \hat{\omega}_m\left(k+1\right)]}{T_s} - J\hat{d}\left(k+1\right) \tag{8}$$

where $\hat{d}(k)$ is identified by the ESO in (6). The diagram of the conventional CCS-MPSC is shown in Fig. 5 based on the control cycle $T_s = 100\ \mu s$. The design of the control law is characterized by the high dynamic performance, but is prone to oscillation at the reference point. Besides, the accurate initial parameters are necessary for (8), which means the mismatched moment of inertia would generate deviation for the torque reference.

C. Analysis of Impact on the Moment of Inertia

To analyze the influence of inertia moment, the state-space equation of the conventional CCS-MPSC with variables $X(k) = \left[\hat{\omega}_m(k) \quad \hat{d}(k) \quad \omega_m(k)\right]^T$ and input $u(k) = T_f(k)$ is designed as follows:

$$\begin{aligned} X\left(k+1\right) &= GX\left(k\right) + Hu\left(k\right) \\ Y\left(k\right) &= CX\left(k\right) + Du\left(k\right) \end{aligned} \tag{9}$$

where

$$G = \begin{bmatrix} 1 - z - T_s\beta_1 & T_s - zT_s & T_s\beta_1 \\ -T_s\beta_2 & 1 & T_s\beta_2 \\ -z & -zT_s & 1 \end{bmatrix}$$

$$H = \begin{bmatrix} 0 & 0 & -T_s/J \end{bmatrix}^T$$

$$C = \begin{bmatrix} 0 & 0 & 1 \end{bmatrix}$$

$$D = \begin{bmatrix} 0 & 0 & 0 \end{bmatrix}$$

$$Y\left(k\right) = \omega_m\left(k\right).$$

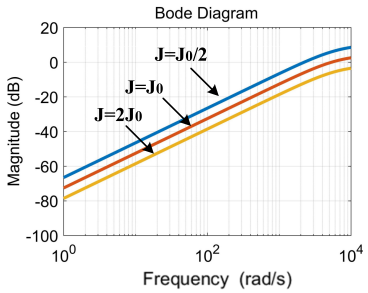

Fig. 6. Bode diagram of (10) with inertia coefficients J_0, $2J_0$, and $0.5J_0$, respectively.

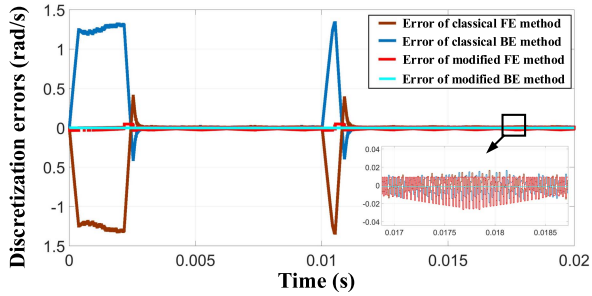

Fig. 7. Discretization errors of several discrete models.

The disturbance transfer function $F(z)$ can be derived as

$$F(z) = \frac{\left[-2z^2 + \left(T_s^2\beta_2 - T_s\beta_1 + 3\right)z + T_s\beta_1 - T_s^2\beta_2 - 1\right]T_s/J}{-2z^3 + (5 - 2T_s\beta_1)z^2 + (3T_s\beta_1 - 2T_s^2\beta_2 - 4)z + T_s^2\beta_2 - T_s\beta_1 + 1}. \tag{10}$$

The corresponding Bode diagrams with different inertia coefficients are shown in Fig. 6. The period is set as $T_s = 100\ \mu$s. The magnitude of the output variable $\omega_m(k)$ is increased with the inertia factor J changed from $J_0/0.5$ to $2J_0$ within input frequency $10^0 \sim 10^4$ rad/s. Thus, the changed inertia coefficient has an impact on the disturbance rejection capability of the conventional CCS-MPSC.

To improve the antidisturbance performance and the robustness against the perturbed the moment of inertia, a novel robust CCS-MPSC is proposed in this article.

IV. Principle of the Proposed Robust CCS-MPSC

A. Modified Discrete Model of Motion Equation

According to (4), the discretization of the rotor angle velocity is essential to implement in the digital processor. Based on a truncated Taylor series expansion, the commonly used discrete methods are classical FE (explicit) method and BE (implicit) method, and are expressed as

$$\begin{aligned} \text{FE}: y_{n+1} &= y_n + hf'(y_n, t_n) \\ \text{BE}: y_{n+1} &= y_n + hf'(y_{n+1}, t_{n+1}) \end{aligned} \tag{11}$$

where $h = t_n - t_{n-1}$ is the step size; and y_n means variable at the nth time step. Meanwhile, the truncated second-order Taylor discretization is shown as

$$y_{n+\Delta n} = y_n + \Delta h f'(y_n, t_n) + \frac{\Delta h^2 f''(y_n, t_n)}{2} \tag{12}$$

where $\Delta h = t_{n+\Delta n} - t_n$.

The FE method is usually used to discretize the motion equation in CCS-MPSC, which has a simple form and is easy to implement. In this article, to reduce the truncated error of the Taylor series expansion, the modified CCS-MPSC is investigated based on the second-order discretization of the mechanical dynamic model. Deriving both sides of the equal sign of (4a), the following equation can be obtained:

$$J\frac{d^2\omega_m}{dt^2} = \frac{dT_e}{dt} - \frac{dT_f}{dt}. \tag{13}$$

Based on (12) and (13), the left side of the equal sign of (13) at k-instant can be derived as follows:

$$\begin{aligned} J\frac{d^2\omega_m}{dt^2} &= \frac{2J}{T_s^2}\left[\omega_m(k+1) - \omega_m(k) - T_s\frac{d\omega_m}{dt}\right] \\ &= \frac{2J}{T_s^2}\left[\omega_m(k+1) - \omega_m(k)\right] - \frac{2}{T_s}\left[T_e(k) - T_f(k)\right]. \end{aligned} \tag{14}$$

By using FE and BE, the right side of (13) at k-instant is decomposed into the following equations, respectively:

$$\frac{dT_e}{dt} - \frac{dT_f}{dt} = \begin{cases} \frac{T_e(k+1) - T_e(k)}{T_s} - \frac{T_f(k+1) - T_f(k)}{T_s} & (15a) \\ \frac{T_e(k) - T_e(k-1)}{T_s} - \frac{T_f(k) - T_f(k-1)}{T_s}. & (15b) \end{cases}$$

In the aforementioned equation, the lump disturbance T_f of adjacent periods is assumed as two different values considering the existence of discrete load. Here, the discretization errors between the sampling angle velocity and computed angle velocity derived at k instant by several kinds of discretized models are investigated, and simulation results are shown in Fig. 7. The parameters of the SPMSM are shown in Table II. The speed reference is set as 1000 r/min at 0 s and changed to 1200 r/min at 0.01 s without load torque. It can be seen the maximum discretization error for the classical FE and BE method are both 1.3 rad/s, which occurs during the dynamic speed tracking process. The error for the modified FE and BE methods are smaller than the classical method at the transient state, which are 0.05 and 0.0005 rad/s, respectively. At steady state, the discretization errors for the classical FE and BE method are

TABLE II
Parameters for the SPMSM

Symbol	Quantity	Parameters
n_r	Rated machine speed	3000 r/min
R_{s0}	Stator resistance	555.22 mΩ
L_{s0}	Inductance	4.02 mH
ψ_{f0}	PM rotor flux	0.05512 V·s
T_e	Rated torque	2.3 N·m
p	Pole pairs	5
j_0	Inertia constant	0.0000853 kg·m^2
V_{dc}	DC-link Voltage	200 V

TABLE III
ANALYSIS OF THE DISCRETE MODELS

Discrete model	Discretization error	
	Steady state	Transient state
Classical FE method	-0.02~0.02 rad/s	1.3 rad/s
Classical BE method	-0.02~0.02 rad/s	1.3 rad/s
Modified FE method	-0.008~0.03 rad/s	0.05 rad/s
Modified BE method	-0.0005~0. 002 rad/s	0.0005 rad/s

around $-0.02\sim0.02$ rad/s, and are almost the same as the one of the modified FE method that is around $-0.008\sim0.03$ rad/s. Besides, the modified BE method has smaller discretization errors than the modified FE method. Table III summarizes the discretization errors of the discrete models.

Based on aforementioned analysis, the modified FE and BE methods are adopted to improve the performance of CCS-MPSC.

B. Novel CCS-MPSC Based on the Modified ESO

By combining (14) and (15b), the modified second-order BE discrete model of rotor angle velocity at *k*-instant is shown as follows:

$$\omega_m\ (k) = \omega_m\ (k-1) + \frac{T_s}{2J}\left[3\Delta T_e\,(k-1) - \Delta T_e\,(k-2)\right] \tag{16}$$

where $\Delta T_e\ (k) = T_e\ (k) - T_f(k)$.

Then, ESO based on the modified second-order FE discrete model can be obtained as

$$\begin{cases} e_\omega\ (k) = \hat{\omega}_m\ (k) - \omega_m\ (k) \\ \hat{\omega}_m\ (k+1) = \hat{\omega}_m\ (k) + T_s[aT_e\ (k) - aT_e\ (k-1) + \hat{r}\ (k) \\ \qquad\qquad -\hat{r}\ (k-1)\ /3] - T_s\beta_1 e_\omega\ (k) \\ \hat{r}\ (k+1) = \hat{r}\ (k) - T_s\beta_2 e_\omega\ (k) \end{cases} \tag{17}$$

where parameter $a = 3/2J$; estimated disturbance $\hat{r}(k) = -T_L/3a$; and gains β_1 and β_2 are similar with (6).

Compared to the conventional ESO, the torque and estimated lump load of the modified ESO (MESO) at the previous instant need to be recorded iteratively and applied as variables to improve the accuracy of the model.

To improve the control performance, this article presents a cost function based on the prediction functional control strategy [31], which is shown as

$$J_c = F^T Q F + R|T_e|^2 \tag{18}$$

where $F = X_r\ (k) - X_p(k) - E(k)$; $X_r(k)$ represents the matrix of speed reference; $X_p(k)$ is matrix of predicted speed value; $E(k)$ is matrix of prediction error; Q and R are coefficients matrix; and T_e is torque term to balance performance.

Comparing to the conventional cost function (7), prediction error and tracking error are both defined as control objective in cost function to reduce the prediction errors. Substituting the variables in (17) into (18), and solving for $\partial J_c/\partial T_e^2 = 0$, the output T_e with minimum J_c can be obtained as follows:

$$T_e = \frac{\left[\omega_m^* - \hat{\omega}_m\,(k+1) + \hat{\omega}_m\,(k) - \omega_m\,(k)\right] aT_s Q}{(a^2 T_s^2 Q + R)}. \tag{19}$$

Due to load torque, which can be identified by (17), the torque reference output of the speed controller is compensated and defined as follows:

$$T_e^* = T_e\ + \hat{T}_f \tag{20}$$

where $\hat{T}_f = -\hat{r}(k+1)/3a$ represents the estimated lump load. The block diagram of the modified ESO is shown in Fig. 8, where parameters $\Gamma = aT_sQ/(a^2T_s^2Q+R)$, $K = T_s\ (1 - 1/3z)$, and $\xi = T_s(3 - z^{-1})/2J$. Q and R denote weighting factors.

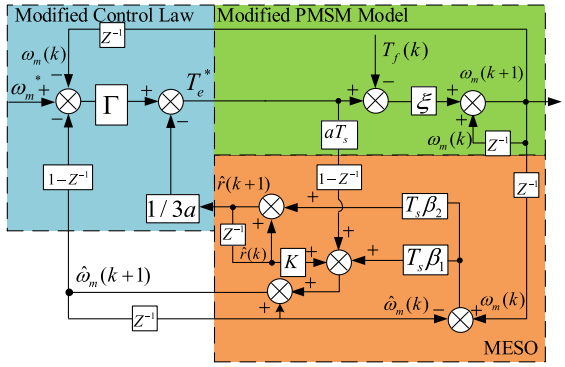

Fig. 8. Block diagram of the proposed CCS-MPSC-based MESO.

It is well known that weighting factor is one of the important parameters that affect the control performance effectively. However, there is no generic theoretical guideline to obtain the weighting factors. To address this issue, several strategies of eliminating weighting factors have been proposed. One common solution is to design the novel cost function with normalized control targets for equal importance control [36]. This method cannot produce optimal results in all the operating conditions. Another strategy is to replace the original variables with a single new variable [37]. For example, MPTC can use a single stator flux variable or voltage vector error to represent the torque error term and stator flux error term [38], [39]. However, this approach cannot include additional objectives and is not suitable for other systems. The separate cost function, in which several control objectives are evaluated sequentially depending on the importance, is an effective method to eliminate weighting factors [40], [41]. Despite of avoiding the use of weighting factors, this method limits the effectiveness of secondary objectives.

While the strategies presented previously eliminate the weighting factor, they still impose a tradeoff between different objectives. To obtain suitable weighting factors Q and R, the discrete Lyapunov function is introduced, which is defined as

$$\begin{cases} V\ (k) = \left[\omega_m^*\ (k) - \hat{\omega}_m\ (k+1) - e\ (k)\right]^2 \\ V\ (k+1) = \left[\omega_m^*\ (k+1) - \hat{\omega}_m\ (k+2) - e\ (k+1)\right]^2 \end{cases} \tag{21}$$

where $e(k) = \omega_m(k) - \hat{\omega}_m(k)$.

The derivative of the Lyapunov function $\Delta V(k)$ can be expressed as follows:

$$\begin{aligned}\Delta V\left(k\right) &= V\left(k+1\right)-V\left(k\right)\\ &= \left[\omega_m^*\left(k+1\right)-\hat{\omega}_m\left(k+2\right)-e\left(k+1\right)\right]^2\\ &\quad -\left[\omega_m^*\left(k\right)-\hat{\omega}_m\left(k+1\right)-e\left(k\right)\right]^2\\ &= \left[\omega_m^*\left(k+1\right)-e\left(k+1\right)\right]^2+\hat{\omega}_m^2\left(k+2\right)\\ &\quad -2\hat{\omega}_m\left(k+2\right)\left[\omega_m^*\left(k+1\right)-e\left(k+1\right)\right]+\hat{\omega}_m^2\left(k+1\right)\\ &\quad -\left[\omega_m^*\left(k\right)-e\left(k\right)\right]^2-2\hat{\omega}_m\left(k+1\right)\left[\omega_m^*\left(k\right)-e\left(k\right)\right].\end{aligned} \tag{22}$$

By defining $\omega_m^*(k+1)\approx\omega_m^*\left(k\right)=\omega_m^*$ and $e(k+1)\approx e(k)$ due to the slow change of the speed variable in adjacent control period, it yields

$$\begin{aligned}\Delta V\left(k\right) &= 2\left[\omega_m^*-e\left(k\right)\right]\left[\hat{\omega}_m\left(k+1\right)-\hat{\omega}_m\left(k+2\right)\right]\\ &\quad +\hat{\omega}_m^2\left(k+2\right)-\hat{\omega}_m^2\left(k+1\right).\end{aligned} \tag{23}$$

According to the discrete motion equation and calculated torque by (19), $\Delta V(k)$ can be derived to as follows:

$$\begin{aligned}\Delta V\left(k\right) &= \left[\hat{\omega}_m\left(k+2\right)-\hat{\omega}_m\left(k+1\right)\right]\left[2e\left(k\right)-2\omega_m^*\right.\\ &\quad \left.+\hat{\omega}_m\left(k+2\right)+\hat{\omega}_m\left(k+1\right)\right]\\ &= \frac{T_s}{J}T_e\left(k+1\right)\\ &\quad \times\left[2e\left(k\right)-2\omega_m^*+2\hat{\omega}_m\left(k+2\right)-\frac{T_s}{J}T_e\left(k+1\right)\right]\\ &= \frac{T_s}{J}\frac{\left[\omega_m^*-\hat{\omega}_m\left(k+2\right)-e\left(k\right)\right]1.5JT_sQ}{\left(1.25T_s^2Q+J^2R\right)}\\ &\quad \times\left[2e\left(k\right)-2\omega_m^*+2\hat{\omega}_m\left(k+2\right)\right]\\ &\quad -\left\{\frac{T_s}{J}\frac{\left[\omega_m^*-\hat{\omega}_m\left(k+2\right)e\left(k\right)\right]1.5JT_sQ}{\left(1.25T_s^2Q+J^2R\right)}\right\}^2.\end{aligned} \tag{24}$$

By defining

$$\frac{3T_s^2Q}{1.25T_s^2Q+J^2R}+\left(\frac{1.5T_s^2Q}{1.25T_s^2Q+J^2R}\right)^2=1 \tag{25}$$

the discrete Lyapunov function can be derived as follows:

$$\Delta V\ \left(k\right)=-\left[\omega_m^*-\hat{\omega}_m\left(k+2\right)-e\left(k\right)\right]^2. \tag{26}$$

Noting that the derivative of the Lyapunov function is negative definite. Thus, the proposed method is asymptotically stable. Assuming weighting factor $Q=2$, another weighting factor $R=5.84$ can be solved.

Depending on the specific application requirements, the weighting factors can be fine tuned. Here, the Bode theorem in the z-domain is adopted to analyze the magnitude feature of weighting Q and R. According to Fig. 8, the state-space equation of proposed CCS-MPSC can be expressed as

$$X\left(k+1\right)=GX\left(k\right)+Hu\left(k\right)$$

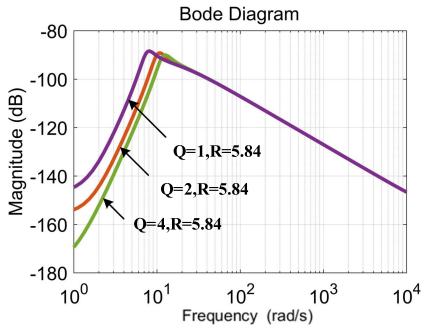

Fig. 9. Magnitude characteristics of the proposed CCS-MPSC with $Q=1,2,4$ and $R=5.84$, respectively.

$$Y\left(k\right)=CX\left(k\right)+Du\left(k\right) \tag{27}$$

where $u\left(k\right)=\ r(k)$, and the matrices of G, H, C, and D are as follows:

$$G=\begin{bmatrix}1+aT_s\left(z-z^{-1}+2\right)-T_s\beta_1 & T_s-\frac{T_s}{3z} & T_s\beta_1-aT_s\Gamma\left(1-z^{-1}\right)\\ -T_s\beta_2 & 1 & T_s\beta_2\\ \frac{T_s\Gamma\left(-3+4z^{-1}-z^{-2}\right)}{2J} & \frac{-z}{3a} & 1-\frac{T_s\Gamma\left(3z^{-1}-z^{-2}\right)}{2J}\end{bmatrix}$$

$$H=\begin{bmatrix}0 & 0 & -\frac{T_s\Gamma\left(3-z^{-1}\right)}{9}\end{bmatrix}^T$$

$$C=\begin{bmatrix}0 & 0 & 1\end{bmatrix}$$

$$D=\begin{bmatrix}0 & 0 & 0\end{bmatrix}$$

$$X\left(k\right)=\begin{bmatrix}\hat{\omega}_m\left(k\right) & \hat{d}\left(k\right) & \omega_m\left(k\right)\end{bmatrix}^T$$

$$Y\left(k\right)=\omega_m\ \left(k\right).$$

Based on (27), the disturbance transfer function $F(z)$ can be derived as (28) shown at the bottom of next page. The Bode diagram is shown in Fig. 9 according to the transfer function $F(z)$. In Fig. 9, the ability of proposed method with $R=5.84$ and $Q=4$ to suppress low-frequency disturbances is much higher than that of the method with $Q=1$ and 2. Meanwhile, the strong antidisturbance performance for the reduced R will perform if the weighting Q is fixed due to the same results being calculated by (19). The conclusions can be used as the guideline to fine tune the weighting factors. To verifythe aforementioned analysis, the simulation and experiment results with different weighting factors are presented in Section V.

C. Inertia Estimation Strategy Based on the Modified MHE

According to the analysis in Section III-C, the changed moment of inertia, which will produce a sudden increase in the estimated load torque during the speed dynamic tracking, has an impact on the accuracy of ESO estimation results. The perturbed estimated load deteriorates the antidisturbance performance of CCS-MPSC [3]. To alleviate the impact of mismatched inertia

parameter, a novel moving horizon estimator (MHE) is designed to identify the moment of inertia online.

The principle of the MHE is same as the CCS-MPC that uses the rolling optimization strategy [32]. The difference is that the MHE is utilized to estimate model parameters, but CCS-MPC is used to track reference. The MHE adopting the FE method with a long horizon is presented in [33]. Unfortunately, the longer the estimation horizon adopted, the higher the computational burden generated. The large order of the matrix is not beneficial for the implementation of the DSP/FPGA. Besides, the stability of the classical MHE has not been presented. To improve the aforementioned solutions, this article proposed a MMHE based on the modified BE method.

The modified second-order BE discrete model of rotor angle velocity at *k*-instant is showed as follows:

$$\omega_m(k) = \omega_m(k-1) + \frac{T_s}{2J}\left[\Delta T_e(k) + \Delta T_e(k-1)\right] \quad (29)$$

where $\Delta T_e(k) = T_e(k) - T_f(k)$; $\omega_m(k)$ represent the sampling value of rotor angle velocity at k instant; and J is the real inertia moment. Since the modified BE model is composed by the state variables of the previous moments, it has unconditionally stable properties regardless of the prediction horizon.

Meanwhile, estimated rotor angle velocity based on the initial moment of inertia J_0 is expressed as

$$\hat{\omega}_m(k) = \hat{\omega}_m(k-1) + \frac{T_s}{2J_0}\left[\Delta T_e(k) + \Delta T_e(k-1)\right] \quad (30)$$

where $\hat{\omega}_m(k)$ is the estimated rotor angle velocity with initial inertia moment J_0 at k instant.

By subtracting (29) from (30), the error model of the moment of inertia can be obtained as

$$\Delta\hat{\omega}_m(k) = \Delta\hat{\omega}_m(k-1) + \left(\frac{T_s}{2J_0} - \frac{T_s}{2J}\right)\left[\Delta T_e(k) + \Delta T_e(k-1)\right] \quad (31)$$

where $\Delta\hat{\omega}_m(k) = \hat{\omega}_m(k) - \omega_m(k)$.

Based on (31), the extended model of the MMHE is designed as

$$\begin{cases} \hat{x}(k) = \hat{x}(k-1) + \lambda(k)\left[u(k) - \hat{f}(k)\right] \\ \hat{f}(k) = \hat{f}(k-1) + \Delta\hat{f}(k-1) \end{cases} \quad (32)$$

where state variable $\hat{x}(k)$ is prediction error $\Delta\hat{\omega}_m(k)$; input $u(k) = T_s/2J_0$; estimated variable $\hat{f}(k) = T_s/2\hat{J}$; $\Delta\hat{f}(k-1)$ is incremental term that summed with $\hat{f}(k-1)$ to obtain $\hat{f}(k)$; and time-varying parameter $\lambda(k) = \Delta T_e(k) + \Delta T_e(k-1)$.

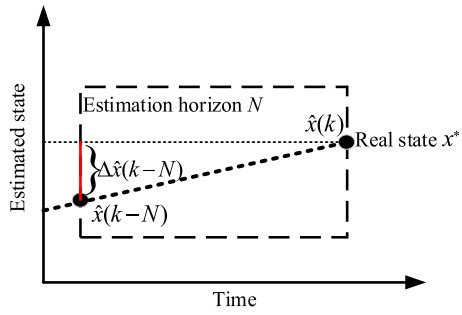

Fig. 10. Diagram of estimating state $\hat{x}(k)$ from $\hat{x}(k-N)$ for MMHE.

And then, the MMHE model at *k-1* instant is expressed as

$$\hat{x}(k-1) = \hat{x}(k-2) + \lambda(k-1)\left[u(k-1) - \hat{f}(k-1)\right]. \quad (33)$$

The moment of inertia can be assumed as a constant value in several adjacent periods due to its slow rate of change. By substituting (33) into (32), (32) is rewritten as follows:

$$\hat{x}(k) = \hat{x}(k-2) + \left[u(k) - \hat{f}(k)\right]\sum_{n=k-2}^{k-1}\lambda(n) \quad (34)$$

where $\sum_{n=k-1}^{k-1}\lambda(n) = \Delta T_e(k) + 2\Delta T_e(k-1) + \Delta T_e(k-2)$. Thus, when the estimation horizon extended to past *N* horizon, the MMHE with an autoregressive model is derived as follows:

$$\hat{x}(k) = \hat{x}(k-N) + \left[u(k) - \hat{f}(k)\right]\sum_{n=k-N}^{k-1}\lambda(n) \quad (35)$$

where $\sum_{n=k-N}^{k-1}\lambda(n) = \Delta T_e(k-N) + 2\sum_{n=k-N+1}^{k-1}\Delta T_e(n) + \Delta T_e(k)$; input $u(k) = T_s/2J_0$; and estimated variable $\hat{f}(k) = \hat{f}(k-N-1) + \Delta\hat{f}(k-N-1)$.

To obtain the accurate estimated value of $\Delta\hat{f}$, the cost function is defined as

$$J_{\text{MHE}} = [x^* - \hat{x}(k)]^2 + \Omega\Delta\hat{f}^2 \quad (36)$$

where reference x^*; and Ω is weighting factor, which determines the speed of estimator convergence. The inertia moment can be identified by solving $\partial J_{\text{MHE}}/\partial\Delta\hat{f} = 0$ for the optimal $\Delta\hat{f}$ corresponding to the minimum cost function J_{MHE}. The estimated $\Delta\hat{f}$ in (35) is expressed as follows:

$$\Delta\hat{f}(k-N-1) = -\frac{H(k-N)\sum_{n=k-N}^{k-1}\lambda(n)}{\left[\sum_{n=k-N}^{k-1}\lambda(n)\right]^2 + \sigma} \quad (37)$$

where $H(k-N) = \hat{x}(k) - \hat{x}(k-N) - [u(k) - \hat{f}(k-N-1)]\sum_{n=k-N}^{k-1}\lambda(n)$; and σ is coefficient. Fig. 10 shows the process of estimating state $\hat{x}(k)$ from $\hat{x}(k-N)$ for the MMHE.

$$F(z) = \frac{z(3T_sz - T_s)\left[-aT_s\Gamma z^2 + (1-T_s\beta_1)z + aT_s\Gamma\right]}{[2JT_s\beta_2z^3 + 9z^2 + (1-3z)3aT_s\Gamma][-aT_s\Gamma z^2 + z + aT_s\Gamma - T_s\beta_1] - \left[(T_s\beta_1 - aT_s - T_s^2\beta_2)z + aT_s + \frac{T_s^2\beta_2}{3}\right][-2JT_s\beta_2z^3 + 3aT_s\Gamma(-3z^2 + 4z - 1)]}. \quad (28)$$

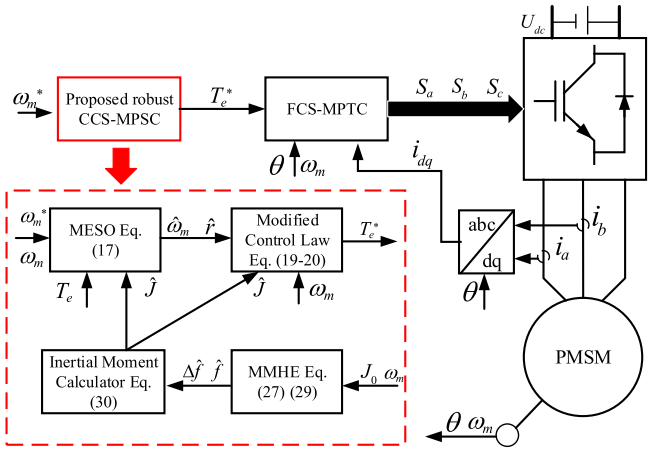

Fig. 11. Block diagram of the proposed robust CCS-MPSC system.

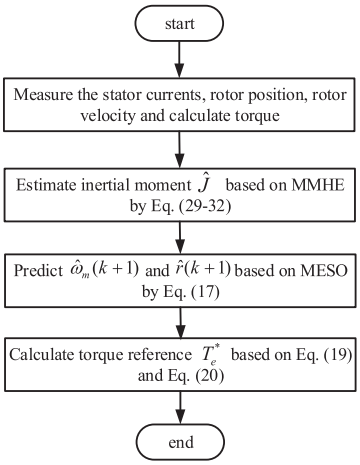

Fig. 12. Flow chart of the proposed robust CCS-MPSC.

According to (37), identified inertia moment at k instant can be obtained as follows:

$$\hat{J} = T_s/2\left[\hat{f}(k-N-1) + \Delta\hat{f}(k-N-1)\right]. \quad (38)$$

The estimated moment of inertia $\hat{J}$ is updating in MESO in (17) and (20) to improve the robustness and disturbance rejection performance of the proposed robust CCS-MPSC. The block diagram and flow chart of the proposed robust CCS-MPSC are shown in Figs. 11 and 12, respectively.

V. Performance Evaluations

As shown in Fig. 11, finite-control set model predictive torque control (FCS-MPTC) is utilized as an inner loop controller due to the advantage of high dynamic performance [43]. The simulation and experimental results are presented to demonstrate the effectiveness of the proposed approach.

A. Simulation Results

To verify the correctness of characteristic analysis on weighting factors R and Q in Section IV-B, MATLAB/Simulink

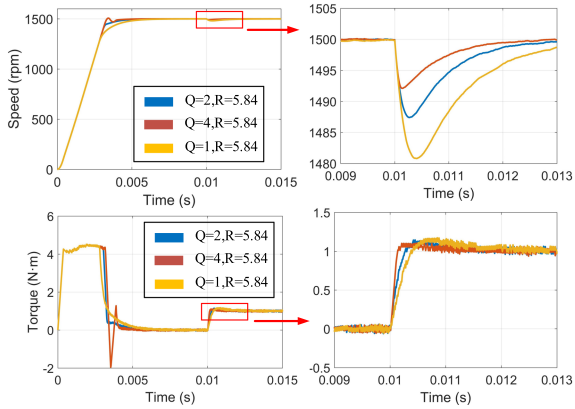

Fig. 13. Simulation results of the proposed CCS-MPSC-based MESO for different weighting factors R and Q under starting operation and encounter load condition.

TABLE IV
Key Design Parameters

Symbol	Quantity	Parameters
Q	Weighting factor in (19)	2
R	Weighting factor in (19)	5.84
σ	Parameter in (31)	4
ω_0	Bandwidth of MESO	4000 rad/s
N^p_{MESO}	Prediction horizon for MESO	1
N^c_{MESO}	Control horizon for MESO	1
N^p_{MMHE}	Prediction horizon for MMHE	3
N^c_{MMHE}	Control horizon for MMHE	1
Simulation conditions 1		
Ref. Speed n [r/min] : n=1500($0 \le t < 0.6$), n=3000($0.6 \le t < 1.4$) Ref. Load torque T_L [N · m]: $T_L = 1(0.2 < t \le 0.4, 0.8 < t \le 1.0)$, $T_L = 2(0.4 < t \le 0.8)$, $T_L = 0(t \le 0.2,\ t > 1.0)$ Ref. Inertia moment j [$\times 10^{-5}$ kg · m^2]: $j = 8.53(0.2 < t \le 0.4, 0.8 < t \le 1.0)$, $j = 10(0.4 < t \le 0.8)$, $j = 12(t \le 0.2,\ t > 1.0)$		
Simulation conditions 2		
Ref. T_L [N · m]	$\begin{cases} 0, 0 < t \le 0.15 \\ 1, 0.15 < t \le 0.25 \\ 2, 0.25 < t \le 0.35 \\ 1, 0.35 < t \le 0.45 \\ 0, 0.45 < t \le 0.6 \end{cases}$	Ref. j [$\times 10^{-5}$ kg · m^2] $\begin{cases} 8.53, 0 < t \le 0.15 \\ 10, 0.15 < t \le 0.25 \\ 12, 0.25 < t \le 0.35 \\ 10, 0.35 < t \le 0.45 \\ 8.53, 0.45 < t \le 0.6 \end{cases}$
Ref. n [r/min]	$\begin{cases} 1000\ , 0 < t \le 0.1 \\ 500\ \ , 0.1 < t \le 0.2 \\ 1000\ , 0.2 < t \le 0.3 \\ 500\ \ , 0.3 < t \le 0.4 \\ 1000, 0.4 < t \le 0.6 \end{cases}$	where t means the simulation time.

results are presented in Fig. 13(a)–(d). The parameters of the SPMSM and prediction horizon have been shown in Tables II and IV. The proposed MESO with weighting factors $Q = 1, 2, 4$ and $R = 5.84$ are conducted. The speed reference is 1500 r/min. At 0.01 s, a sudden load torque of 1 N · m is added.

For the motor start condition in Fig. 13, the feedback value of speed reaches the reference value faster for $Q = 4,\ R = 5.84$ (case 3) than $Q = 2,\ R = 5.84$ (case 2) and $Q = 1,\ R = 5.84$ (case 1). Meanwhile, the overshoots are 6 r/min (case 3), 1 r/min (case 1), and 0 r/min (case 2) in starting condition, respectively. Besides, for the encountering load condition, the drop amplitudes of speed at 0.01 s are 8, 12, and 20 r/min

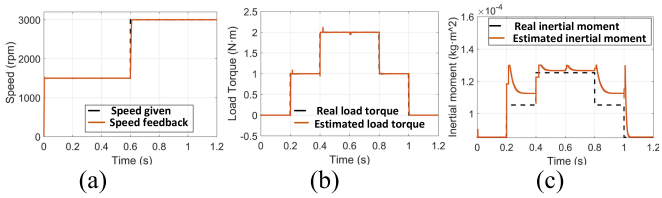

Fig. 14. Simulation results of the proposed robust CCS-MPSC based on condition 1. (a) Speed feedback. (b) Estimated load torque. (c) Estimated inertia moment.

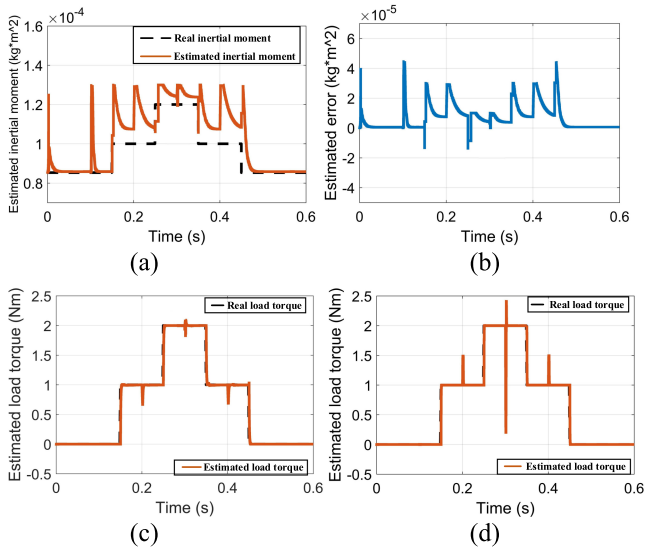

Fig. 15. Simulation results of the proposed robust CCS-MPSC based on condition 2. (a) Estimated inertia moment. (b) Estimation error between real inertia moment and estimated inertia moment. (c) Estimated load torque with MMHE. (d) Estimated load torque without MMHE.

for cases 3, 2, and 1, respectively. Thus, better antidisturbance performance is presented for $Q = 4$. But the drawback is that the increased overshoot is simultaneously presented with the increased Q. Therefore, the demonstrations shown in Fig. 13 are consistent with the results of the previous theoretical analysis in Fig. 9. The weighting factors need to be fine-tuned depending on the specific application demands.

To verify the effectiveness of proposed method, simulation results of the proposed robust CCS-MPSC are presented in Fig. 14(a)–(c). Simulation results shown in Fig. 15(a)–(d) explore the effect of estimated inertia on the changed speed and load torque. To investigating the superior performance of the proposed robust CCS-MPSC comparing to the conventional CCS-MPSC, simulation results are shown in Fig. 16(a)–(d). The corresponding conditions and key design parameters are shown in Table IV. The weighting factors Q and R are set to 2 and 5.84, respectively. The parameter σ is 4 and bandwidth of MESO is 4000 rad/s by referring to [19] and [33]. The prediction horizon and control horizon for MESO are both set as 1 due to the utilization of the deadbeat strategy in (19). Meanwhile, the

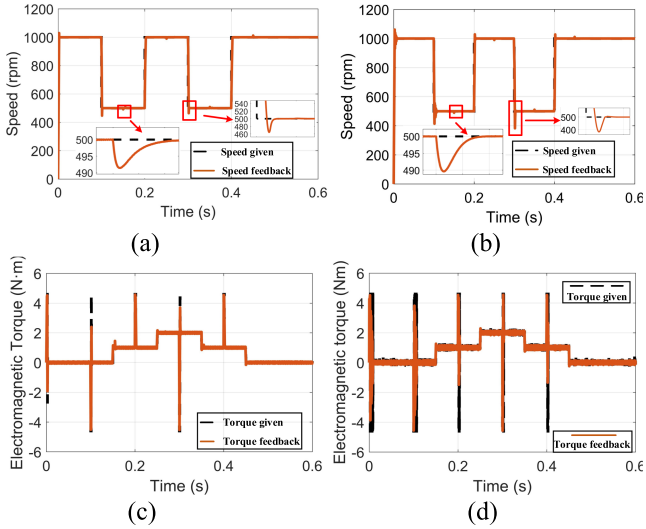

Fig. 16. Simulation results of the proposed robust CCS-MPSC and conventional CCS-MPSC based on condition 2. (a) Speed feedback for the proposed robust CCS-MPSC. (b) Speed feedback for the conventional CCS-MPSC. (c) Torque feedback for the proposed robust CCS-MPSC. (d) Torque feedback for the conventional CCS-MPSC.

prediction horizon for the MMHE is set as 3 to improve the accuracy and convergence rate, and the control horizon is set to 1.

In Fig. 14, it can be seen that the speed feedback tracks reference quickly without overshoots at 0.6 s. The estimated load torque of MESO follows the given load torque quickly with the bandwidth 4000 rad/s. The estimated inertia moment tracks the perturbed real inertia moment, which is not affected by changed load torque and speed. Due to small magnitude of inertia moment, the minimum accuracy of estimated inertia moment is 95% ($0.2 < t \leq 0.4,\ 0.8 < t \leq 1$).

In Fig. 15(a), it can be clearly seen that a convergence process of the estimated inertia moment is presented when the permanent-magnet synchronous motor (PMSM) is working in the transient state. The estimated inertia moment would converge to the real inertia moment within 0.04 s. According to Fig. 15(b), estimation error rates for the final convergent value are 0.55% (0∼0.15 s and 0.45∼0.6 s), 7.2% (0.15∼0.25 s and 0.35∼0.45 s), and 3.1% (0.25∼0.35 s), respectively. Thus, the accurate estimated inertia moment can be obtained by the proposed MMHE. According to Fig. 15(c)–(d), due to the large errors between real inertia moment and initial inertia moment, large estimation error of load torque is caused during the speed tracking process for the CCS-MPSC without MMHE, especially errors of 1.8 $\mathrm{N \cdot m}$ at 0.3 s. Based on the aforementioned, the effectiveness of the proposed MMHE is verified. And the MMHE is beneficial for MESO to identify a more accurate load torque value.

The comparison results between the proposed robust CCS-MPSC and conventional CCS-MPSC are shown in Fig. 16. According to Fig. 16(a) and (b), speed ripples have occurred generally in control points for the conventional CCS-MPSC. And the maximum overshoot is 96 r/min at 0.3 s in Fig. 16(b).

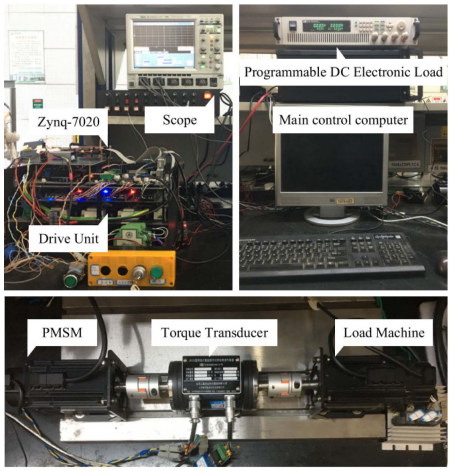

Fig. 17. Block diagram of the test bench based on zynq 7020.

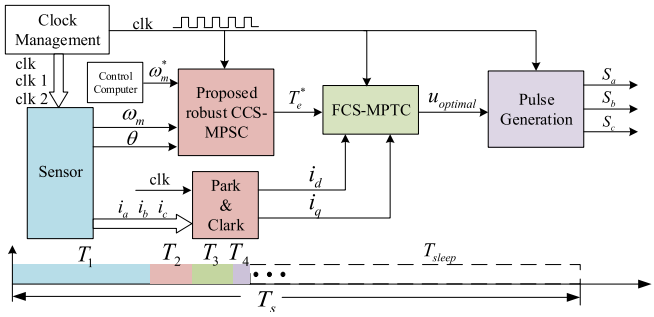

Fig. 18. Algorithm architecture implemented in FPGA.

Compared to the conventional CCS-MPSC, speed feedback can be control smoothly and quickly for the proposed CCS-MPSC in Fig. 16(a), and overshoot are 54 and 35 r/min at 0.1 and 0.3 s, respectively. Meanwhile, when encountering 1-N · m load torque, drop amplitude of speed is 8 r/min at 0.15 s for the proposed CCS-MPSC, while the conventional CCS-MPSC is 10 r/min. Thus, proposed robust CCS-MPSC shows better antidisturbance performance. Moreover, better torque tracking performance is presented for the proposed robust CCS-MPSC according to Fig. 16(c) and (d). Based on the aforementioned, it can be concluded that the proposed robust CCS-MPSC has the advantages of small overshoot and high dynamic performance, strong disturbance rejection ability in speed adjustment, and encountering load conditions when compared with the conventional CCS-MPSC.

B. Experiment Results

A test bench based on the ZYNQ7020 chip is utilized to verify the effectiveness of the proposed robust CCS-MPSC. The experimental prototype is shown in Fig. 17. To reduce the computational time, the proposed method is implemented by the programmable logic (PL) of ZYNQ 7020, which is executed by the parallel pipeline execution architecture. Fig. 18 illustrates the algorithm parallel architecture implemented in the FPGA. The clock management module outputs several clock signals with different frequency to control the calculation frequencies of the different controllers. The key parameters are transferred to the proposed speed controller by the main control computer. The FPGA resource utilization and execution time are presented in Table V. Noting that algorithm requires a short execution time and that there still exist free resources available. Meanwhile, the control period for current loop and speed loop are set as 100 and 200 μs, respectively.

TABLE V
KEY FPGA DESIGN DETAILS

Parameters	Timing	Resource	Utilization
clk for FPGA	0.02 μs	LUT	51.29 %
clk 1 for current-loop	100 μs	LUTRAM	5.07 %
clk 2 for speed-loop	200 μs	FF	26.07 %
T_1	64 clks(1.28 μs)	BRAM	35.71 %
T_2	21 clks(0.42 μs)	DSP	90 %
T_3	20 clks(0.4 μs)	BUFG	12.5 %
T_4	8 clks(0.16 μs)	IO	32.8 %
T_{sleep}	>92 μs		

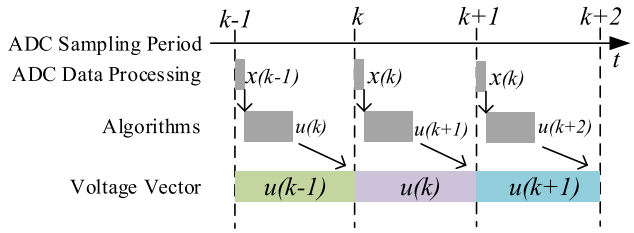

Fig. 19. Time sequence of the proposed CCS-MPSC.

The sampling phase current variables of the PMSM are obtained by the high-speed AD7606 chip, which has maximum 200 kS/s. To obtain the sampled signal in every control period, the update frequency of sampled variable in the current loop is 10 kHz. In addition, the update frequency of the sampled variable in the speed loop is 5 kHz. Fig. 19 shows the time sequence of the proposed method. Since the time required for the analog-to-digital converter (ADC) data processing is much shorter than the time required for a single control cycle, the data processing does not affect the control performance and can be ignored. Meanwhile, due to the deadbeat strategy, the digital delay can be compensated when the prediction horizon is 1. The rotor position and speed variables are solved by the sampled pulse number of the incremental encoder, which is integrated with the PMSM. The tested PMSM is mechanically connected to the same load PMSM and the torque transducer by a coupling. The characteristics of discrete 1-cos load and pump load are simulated by the load PMSM.

1) Weighting Factors $Q = 2$ and $R = 20$: First, the weighting factors are set as $Q = 2$ and $R = 20$. Other key control parameters are linked with Table IV. The experiments at rated speed 3000 r/min are conducted to demonstrate the effectiveness

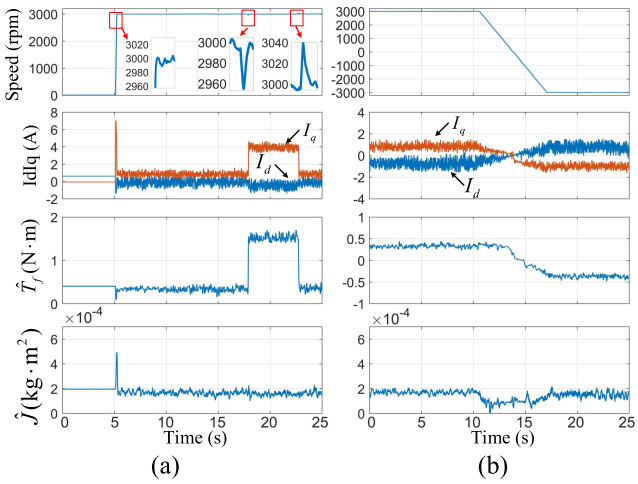

Fig. 20. Experiment results of the proposed robust CCS-MPSC. (a) Performances under starting operation and changing load torque condition. (b) Performances under speed reversal from 3000 to -3000 r/min without load.

of the proposed method, and corresponding results are shown in Fig. 20(a) and (b). In Fig. 20(a), step speed change from 0 to 3000 r/min for the proposed method in 0.1 s without overshoot. An initial load torque is used to simulate the input shaft load of the axial-piston pump. When encountering 1-N · m load torque, the settling time and speed overshoot are 0.07 s and 41 r/min, respectively. The corresponding estimated lump load torque $\hat{T}_f$ changes to 1.3 N · m at 21 s. The estimated inertia moment $\hat{J}$ can be converged to 1.7 $\times 10^{-4}$ kg · m^2, which is consistent with the theoretical value for two same PMSM connected by a coupling. According to Fig. 17(b), the effectiveness of speed reversal in the full speed range is verified. Based on the aforementioned, the effectiveness and stability of the proposed robust CCS-MPSC are verified by experiment results.

Second, comparison experiment results in steady state and transient state for the proposed robust CCS-MPSC and conventional CCS-MPSC are presented in Fig. 21(a)–(d). The reference speed is 1000 r/min. From Fig. 21(a) and (b), it can be clearly seen that proposed method has a smaller overshoot than the conventional CCS-MPSC. The estimated lump load torque is different when the motor start, while the proposed method demonstrates a more accurate value of 0.3 N · m, compared with the conventional method with 1.8 N · m. Besides, a smaller q-current ripple is shown in the steady state for the proposed method with the modified model. From Fig. 21(c) and (d), the proposed robust CCS-MPSC have a smaller overshoot and a shorter settling time than the conventional CCS-MPSC when encounter 1-N · m load torque. Moreover, the control errors caused by inaccurate inertia moment is reduced in the proposed method.

Third, by disconnecting the mechanical connection of the tested PMSM and load PMSM, speed comparison results with changed inertia moment J for the proposed method and conventional method are shown in Fig. 22(a) and (b). When step speed change from 0 to 1000 r/min with changed J, speed ripples are generated at the reference point, and the overshoot is 130 r/min

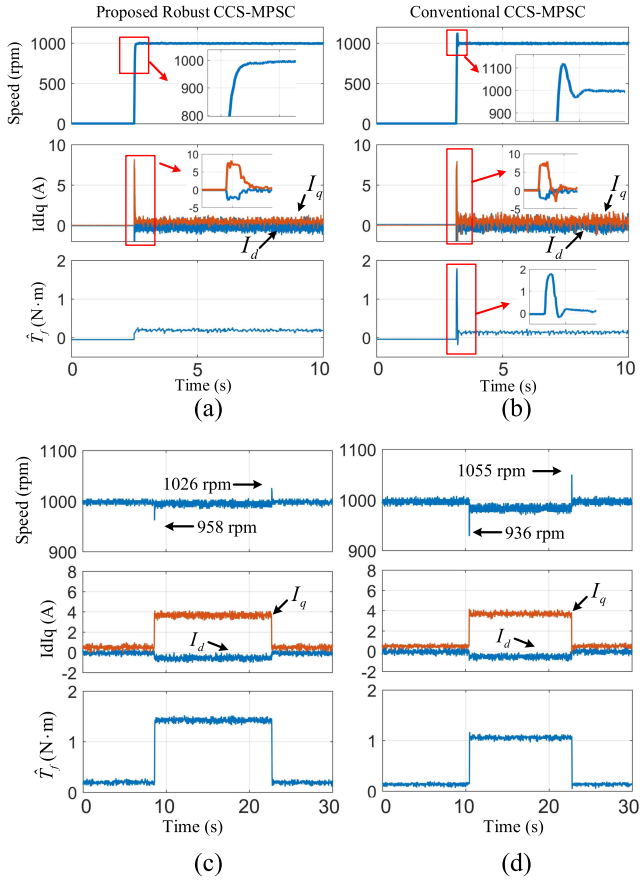

Fig. 21. Experimental results of the proposed robust CCS-MPSC and conventional CCS-MPSC. (a) Starting operation (0–1000 r/min) for the proposed method. (b) Starting operation (0–1000 r/min) for the conventional method. (c) Encountering 1-N · m load torque during 1000 r/min for the proposed method. (d) Encountering 1-N · m load torque during 1000 r/min for the conventional method.

for the conventional method. Meanwhile, a large current ripple is generated in the steady state. Comparing with the conventional method, the proposed method improves the control performance by identifying real-time moments of inertia, which is shown in Fig. 22(c).

Finally, the experimental results of step speed changes with discrete cos load torque, which simulated the working conditions in the EHA, are shown in Fig. 23(a)–(g). Considering the maneuverability of the aircraft, the speed reference changes once every 2 s. The discrete cos load torque with the amplitude of 0.5 N · m is changing with the speed reference to test the speed tracking performance of the proposed method. From details in Fig. 23(c) and (d), the proposed method has a better tracking performance in the transient state and steady state, while the speed ripple is ± 4 r/min in steady state and speed drop is 42 r/min at 5.2 s, compared with the conventional method with ± 7 and 60 r/min. Besides, the conventional method shows a tracking error of 10 r/min. In Fig. 23(e)–(f), the proposed method has a smaller estimated lump load torque ripples when speed reference changes, while the load torque ripple is 0.1 N · m, compared with the conventional method with 0.15 N · m. In Fig. 23(g), estimated inertia moment can be converged to real

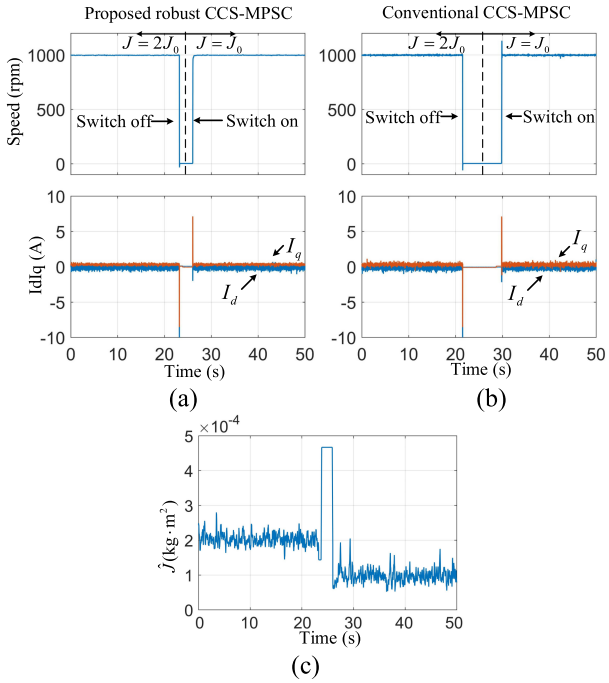

Fig. 22. Experimental results of the proposed robust CCS-MPSC and conventional CCS-MPSC. (a) Starting operation (0–1000 r/min) for the proposed method with the changed J. (b) Starting operation (0–1000 r/min) for the conventional method with changed J. (c) Estimated inertia moment J for the proposed method.

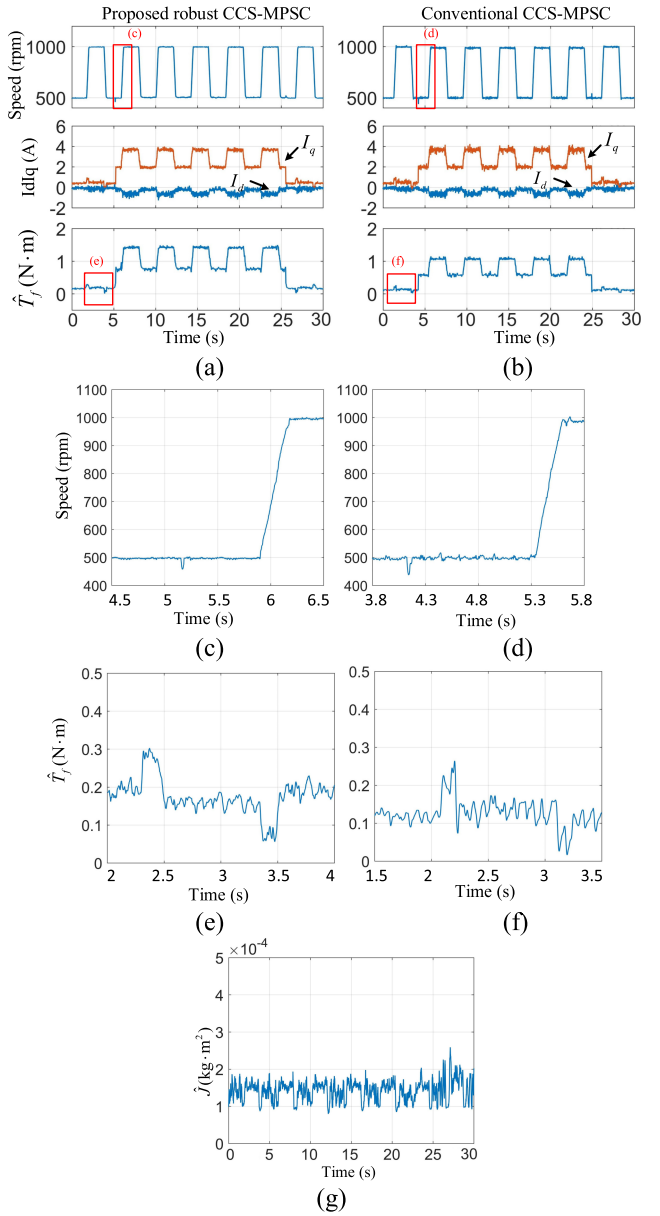

Fig. 23. Step speed changed by 500 r/min with discrete cos load torque. (a) Proposed robust CCS-MPSC. (b) Conventional CCS-MPSC. (c) Zoom-in transient-state performance of the proposed robust CCS-MPSC. (d) Zoom-in transient-state performance of the conventional CCS-MPSC. (e) Zoom-in estimated lump load torque $\hat{T}_f$ for the proposed robust CCS-MPSC. (f) Zoom-in estimated lump load torque $\hat{T}_f$ for the conventional CCS-MPSC. (g) Estimated inertia moment J for the proposed method.

inertia moment in transient state. Thus, it can be concluded that the proposed robust CCS-MPSC demonstrates better transient-state and steady-state performances than the conventional CCS-MPSC.

2) Weighting Factors $Q = 2$ and $R = 5.84$: As the weighting factors are changed to $Q = 2$ and $R = 5.84$, several experimental results are also conducted to verify the effectiveness and present the superior control performance. First, the control performances under the speed response 0–1500–3000-r/min operating and speed reversal from 1000 to -1000 r/min with no load are shown in Fig. 24(a) and (b). It is clearly seen that the fast speed tracking performance without overshoot is demonstrated. The corresponding switching frequency of the proposed method is within 8–10 kHz. In Fig. 24(c) and (d), the experimental results for the speed reversal from 1000 to -1000 r/min are presented. The speed ripples are $+1 \sim -5$ r/min. The corresponding switching frequency of the proposed method is within 6–10 kHz. Thus, the effectiveness of the proposed method with weighting $Q = 2$ and $R = 5.84$ is verified.

And then, the experimental results under low-speed and zero speed with nominal torque are shown in Fig. 25(a) and (b). Noting that amplitude of speed ripple is ± 5 r/min. Meanwhile, the q-axis current presents 0.8-A current ripples. The speed regulation can be achieved from low-speed 100 to -100 r/min. In addition, the zero speed with nominal torque operation is verified.

Besides, the experiments comparing the proposed method and proportional-integral (PI)-based controller are conducted. The speed reference is 1000 r/min encountering 1-N•m load torque. Fig. 26(a) and (b) show the experiment comparisons. The speed drop of the proposed CCS-MPSC is 38 r/min while PI-based controller is 52 r/min as load torque change from 0 to 1 N•m. When load torque changes from 1 to 0 N•m, speed overshoot of the proposed method is smaller than that of PI-based controller. Thus, the proposed CCS-MPSC presents stronger load rejection

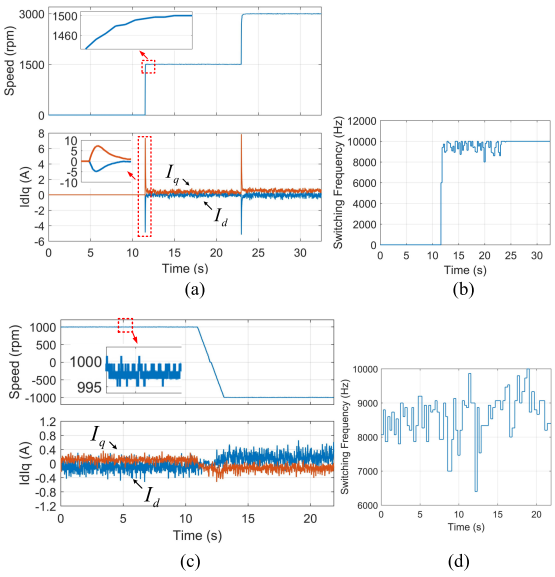

Fig. 24. Experiment results of the proposed CCS-MPSC under speed response 0–1500–3000 r/min without load (operation 1) and speed reversal from 1000 to -1000 r/min with no load (operation 2). (a) Speed and *dq*-axes current for operation 1. (b) Switching frequency for operation 1. (c) Speed and *dq*-axis current for operation 2. (d) Switching frequency for operation 2.

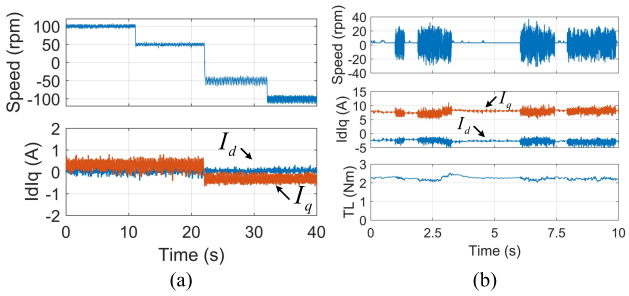

Fig. 25. Experiment results for the proposed method under low speed and zero speed. (a) Low speed within 100∼-100 r/min. (b) Zero speed with nominal torque.

ability. Meanwhile, according to Figs. 21(c) and 26(a), the antidisturbance performance for weighting factors $Q = 2$ and $R = 5.84$ is better than that of $Q = 2$ and $R = 20$.

Furthermore, the robustness against mismatched inertial moment are tested for both PI-based controller and the proposed method. The control performance is shown in Fig. 27(a) and (b). The speed PI controller and proposed CCS-MPSC keep the same parameters under different inertial moment conditions (proportion parameters and integral parameters are 0.032 and 0.001, respectively). Noting that the speed ripples of the PI-based controller are ±20 r/min, and large *dq*-current ripples in steady state. For the proposed CCS-MPSC, the speed ripple is ±5 r/min and current ripple is ±1 A. The large current ripples will cause hardware damage and control system instability. Therefore, the proposed CCS-MPSC performs better in terms of robustness and reliability than the PI-based controller.

Finally, the comparisons between the proposed robust CCS-MPSC and conventional CCS-MPSC are demonstrated in

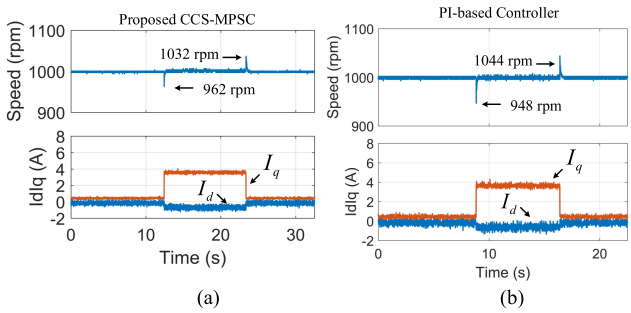

Fig. 26. Experimental results for comparison between the proposed CCS-MPSC and PI-based controller under 1000 r/min encountering 1-N·m load. (a) Proposed CCS-MPSC. (b) PI-based speed controller.

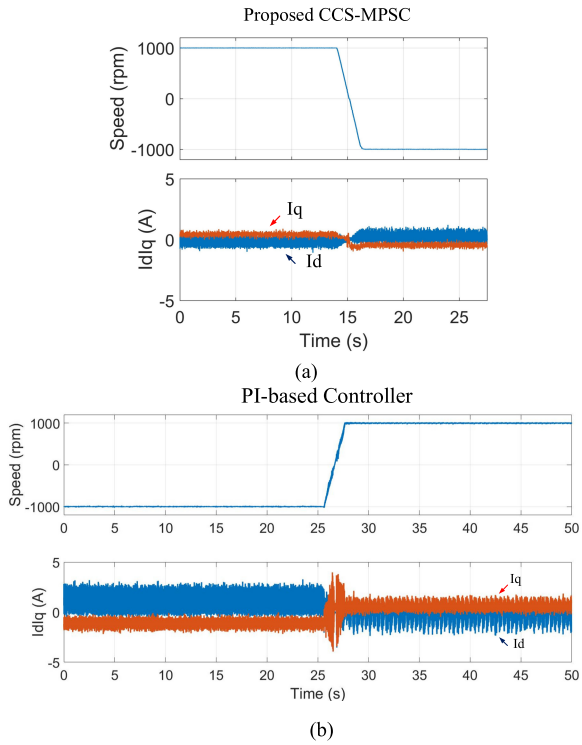

Fig. 27. Experiment results for speed from 1000 to −1000 r/min with 2.25J and no-load. (a) Proposed robust CCS-MPSC. (b) PI-based controller.

Fig. 28(a) and (b). Noting that the speed overshoot of the proposed robust CCS-MPSC is much smaller than that of the conventional CCS-MPSC under the mismatched inertial moment condition. Thus, the speed predictive error for the proposed method will be reduced. The maximum speed predictive errors for the proposed method and conventional method are 26 and 450 r/min, respectively. In addition, the estimated error of load torque for the proposed method is 0.3 N•m, while the conventional method is 1.5 N•m when motor speed changes. Thus, due to the smaller predictive error, the proposed method performs better in terms of the robustness and reliability compared with the conventional method.

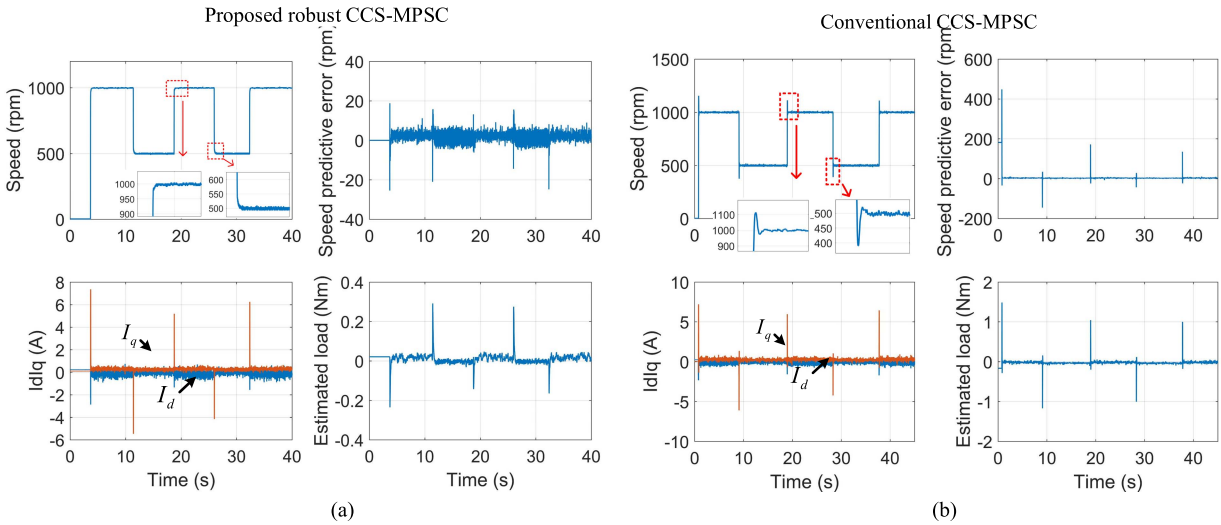

Fig. 28. Experimental results of the proposed robust CCS-MPSC and conventional CCS-MPSC with $J_{\text{real}} = 0.5J_{\text{initial}}$. (a) Proposed robust CCS-MPSC. (b) Conventional CCS-MPSC.

VI. Conclusion

This article propose a novel robust CCS-MPSC based on the MESO and MMHE to enhance the robustness and antidisturbance of the PMSM variable speed drive system in the EHA. Based on the investigation of the external (i.e., aerodynamic load) and internal (i.e., pump load and perturbed inertia moment) disturbances in the EHA, the load characteristics of the PMSM drive system are presented. To improve the accuracy of the CCS-MPSC discrete model, a modified second-order discrete model based on the FE and BE methods is proposed. To enhance the speed tracking capability of CCS-MPSC, the MESO and MMHE are presented. These modifications take into account the disturbed inertia moments and unknown disturbances in the EHA. The enhanced control law is designed based on the MESO. The magnitude characteristics of the proposed CCS-MPSC based on the MESO are investigated by the Bode integral theorem in the z-domain and verified by simulation. According to simulation and experimental results, the suggested robust CCS-MPSC performs better at speed tracking in both steady-state and transient conditions.

References

[1] W. Cao, B. C. Mecrow, G. J. Atkinson, J. W. Bennett, and D. J. Atkinson, "Overview of electric motor technologies used for more electric aircraft (MEA)," *IEEE Trans. Ind. Electron.*, vol. 59, no. 9, pp. 3523–3531, Sep. 2012.

[2] J. C. Mar´e, *Aerospace Actuators, Signal-by-Wire and Power-by-Wire*, vol. 2. Hoboken, NJ, USA: Wiley, 2017.

[3] C. Liu, G. Luo, Z. Chen, and W. Tu, "Finite-time convergent multiple disturbance rejection control for electromechanical actuators," *IEEE Trans. Power Electron.*, vol. 36, no. 6, pp. 6863–6878, Jun. 2021, doi: 10.1109/TPEL.2020.3036410.

[4] Z. Haifeng, X. Jian, G. Wenliang, and Z. Li, "Modeling and simulation of EHA system based on fuzzy adaptive PID control," in *Proc. IEEE 3rd Inf. Technol. Mechatronics Eng. Conf.*, 2017, pp. 750–753.

[5] F. Plestan, Y. Shtessel, V. Brégeault, and A. Poznyak, "Sliding mode control with gain adaptation—Application to an electropneumatic actuator," *Control Eng. Pract.*, vol. 21, no. 5, pp. 679–688, 2013.

[6] T. Röben and E. Stumpf, "An innovative all-active hybrid actuation system," in *Proc. 15th AIAA Aviation Technol., Integration, Operations Conf.*, 2015, pp. 22–26.

[7] J. Rodriguez et al., "Latest advances of model predictive control in electrical drives. Part I: Basic concepts and advanced strategies," *IEEE Trans. Power Electron.*, vol. 37, no. 4, pp. 3927–3942, Apr. 2022.

[8] J. Rodriguez et al., "Latest advances of model predictive control in electrical drives. Part II: Applications and benchmarking with classical control methods," *IEEE Trans. Power Electron.*, vol. 37, no. 5, pp. 5047–5061, May 2022.

[9] M. Liu, K. W. Chan, J. Hu, W. Xu, and J. Rodriguez, "Model predictive direct speed control with torque oscillation reduction for PMSM drives," *IEEE Trans. Ind. Inform.*, vol. 15, no. 9, pp. 4944–4956, Sep. 2019.

[10] X. Gao, M. Abdelrahem, C. M. Hackl, Z. Zhang, and R. Kennel, "Direct predictive speed control with a sliding manifold term for PMSM drives," *IEEE J. Emerg. Sel. Topics Power Electron.*, vol. 8, no. 2, pp. 1258–1267, Jun. 2020.

[11] P. Kakosimos and H. Abu-Rub, "Predictive speed control with short prediction horizon for permanent magnet synchronous motor drives," *IEEE Trans. Power Electron.*, vol. 33, no. 3, pp. 2740–2750, Mar. 2018.

[12] R. Kennel and A. Linder, "Predictive control of inverter supplied electrical drives," in *Proc. IEEE 31st Annu. Power Electron. Specialists Conf.*, 2000, vol. 2, pp. 761–766.

[13] A. A. Ahmed, B. K. Koh, and Y. I. Lee, "A comparison of finite control set and continuous control set model predictive control schemes for speed control of induction motors," *IEEE Trans. Ind. Inform.*, vol. 14, no. 4, pp. 1334–1346, Apr. 2018.

[14] L. He, F. Wang, and D. Ke, "FPGA-based sliding-mode predictive control for PMSM speed regulation system using an adaptive ultralocal model," *IEEE Trans. Power Electron.*, vol. 36, no. 5, pp. 5784–5793, May 2021.

[15] Z. Li, F. Wang, D. Ke, J. Li, and W. Zhang, "Robust continuous model predictive speed and current control for PMSM with adaptive integral sliding-mode approach," *IEEE Trans. Power Electron.*, vol. 36, no. 12, pp. 14398–14408, Dec. 2021.

[16] Y. Zhang, Z. Yin, W. Li, J. Liu, and Y. Zhang, "Adaptive sliding-mode-based speed control in finite control set model predictive torque control for induction motors," *IEEE Trans. Power Electron.*, vol. 36, no. 7, pp. 8076–8087, Jul. 2021.

[17] F. Wang and L. He, "FPGA-based predictive speed control for PMSM system using integral sliding-mode disturbance observer," *IEEE Trans. Ind. Electron.*, vol. 68, no. 2, pp. 972–981, Feb. 2021.

[18] L. Qu, W. Qiao, and L. Qu, "An extended-state-observer-based sliding-mode speed control for permanent-magnet synchronous motors," *IEEE J. Emerg. Sel. Topics Power Electron.*, vol. 9, no. 2, pp. 1605–1613, Apr. 2021.

[19] Y. Zhang, J. Jin, and L. Huang, "Model-free predictive current control of PMSM drives based on extended state observer using ultralocal model," *IEEE Trans. Ind. Electron.*, vol. 68, no. 2, pp. 993–1003, Feb. 2021.
[20] F. Wang, D. Ke, X. Yu, and D. Huang, "Enhanced predictive model based deadbeat control for PMSM drives using exponential extended state observer," *IEEE Trans. Ind. Electron.*, vol. 69, no. 3, pp. 2357–2369, Mar. 2022.
[21] L. Yan, F. Wang, M. Dou, Z. Zhang, R. Kennel, and J. Rodríguez, "Active disturbance-rejection-based speed control in model predictive control for induction machines," *IEEE Trans. Ind. Electron.*, vol. 67, no. 4, pp. 2574–2584, Apr. 2020.
[22] Y. Zuo, J. Mei, X. Zhang, and C. H. T. Lee, "Simultaneous identification of multiple mechanical parameters in a servo drive system using only one speed," *IEEE Trans. Power Electron.*, vol. 36, no. 1, pp. 716–726, Jan. 2021.
[23] M. Kopf, E. Bullinger, H.-G. Giesseler, S. Adden, and R. Findeisen, "Model predictive control for aircraft load alleviation: Opportunities and challenges," in *Proc. Annu. Amer. Control Conf.*, 2018, pp. 2417–2424.
[24] D. Balatti, H. Haddad Khodaparast, M. I. Friswell, and M. Manolesos, "Improving wind tunnel '1-cos' gust profiles," American Institute of Aeronautics and Astronautics, doi: 10.2514/6.2022-2485.
[25] F. Hoblit, Gust Loads on Aircraft: Concepts and Applications, Jan. 1, 1988, doi: 10.2514/4.861888.
[26] V. S. Mehta and N. D. Manring, "Torque ripple attenuation of an axial piston pump by continuous swash plate adjustment," in *Proc. ASME Int. Mech. Eng. Congr. Expo.. Fluid Power Syst. Technol.*, 2005, pp. 147–155.
[27] S. Wang, "Novel piston pressure carryover for dynamic analysis and designs of the axial piston pump," *J. Dyn. Syst. Meas. Control*, vol. 135, no. 2, Dec. 2012, Art. no. 024504.
[28] C. Shi et al., "Variable load failure mechanism for high-speed load sensing electro-hydrostatic actuator pump of aircraft," *Chin. J. Aeronaut.*, vol. 31, no. 5, pp. 949–964, 2018.
[29] N. Simonsen, E. M. Sørensen, M. V. Binsbergen-Galán, S. F. H. Kleine, M. H. Nielsen, and L. Schmidt, "Noise attenuation in a secondary controlled electro-hydraulic actuator using an extended Kalman filter," in *Proc. ASME/BATH Symp. Fluid Power Motion Control*, 2021, Art. no. V001T01A018.
[30] P. Vaclavek, P. Blaha, and I. Herman, "AC drive observability analysis," *IEEE Trans. Ind. Electron.*, vol. 60, no. 8, pp. 3047–3059, Aug. 2013.
[31] H. Liu and S. Li, "Speed control for PMSM servo system using predictive functional control and extended state observer," *IEEE Trans. Ind. Electron.*, vol. 59, no. 2, pp. 1171–1183, Feb. 2012.
[32] F. Toso, D. Da Rù, P. Alotto, and S. Bolognani, "A moving horizon estimator for the speed and rotor position of a sensorless PMSM drive," *IEEE Trans. Power Electron.*, vol. 34, no. 1, pp. 580–587, Jan. 2019.
[33] G. Pei, J. Liu, X. Gao, W. Tian, L. Li, and R. Kennel, "Deadbeat predictive current control for SPMSM at low switching frequency with moving horizon estimator," *IEEE J. Emerg. Sel. Topics Power Electron.*, vol. 9, no. 1, pp. 345–353, Feb. 2021.
[34] J. Wang, Y. Liu, J. Yang, F. Wang, and J. Rodríguez, "Adaptive integral extended state observer based improved multi-step FCS-MPCC for PMSM," *IEEE Trans. Power Electron.*, vol. 38, no. 9, pp. 11260–11276, Sep. 2023, doi: 10.1109/TPEL.2023.3279856.
[35] Y. Wang, S. Fang, and D. Huang, "An improved model-free active disturbance rejection deadbeat predictive current control method of PMSM based on data-driven," *IEEE Trans. Power Electron.*, vol. 38, no. 8, pp. 9606–9616, Aug. 2023, doi: 10.1109/TPEL.2023.3280013.
[36] A. Yang and Z. Lu, "Multiscalar model-based predictive torque control without weighting factors and current sensors for induction motor drives," *IEEE J. Emerg. Sel. Topics Power Electron.*, vol. 10, no. 5, pp. 5785–5797, Oct. 2022.
[37] T. He, M. Wu, R. P. Aguilera, D. D.-C. Lu, Q. Liu, and S. Vazquez, "Low computational burden model predictive control for single-phase cascaded H-bridge converters without weighting factor," *IEEE Trans. Ind. Electron.*, vol. 70, no. 3, pp. 2396–2406, Mar. 2023.
[38] M. Khalilzadeh and S. Vaez-Zadeh, "A robust predictive torque and flux control for IPM motor drives without a cost function," *IEEE Trans. Power Electron.*, vol. 36, no. 7, pp. 8067–8075, Jul. 2021.
[39] M. F. Elmorshedy, W. Xu, S. M. Allam, J. Rodriguez, and C. Garcia, "MTPA-based finite-set model predictive control without weighting factors for linear induction machine," *IEEE Trans. Ind. Electron.*, vol. 68, no. 3, pp. 2034–2047, Mar. 2021.
[40] D. Xiao, M. P. Akter, K. Alam, R. Dutta, S. Mekhilef, and M. F. Rahman, "Cascaded predictive flux control for a 3-L active NPC fed IM drives without weighting factor," *IEEE Trans. Energy Convers.*, vol. 36, no. 3, pp. 1797–1807, Sep. 2021.
[41] N. S. P. Musunuru and S. Srirama, "Cascaded predictive control of a single power supply-driven four-level open-end winding induction motor drive without weighting factors," *IEEE J. Emerg. Sel. Topics Power Electron.*, vol. 9, no. 3, pp. 2858–2867, Jun. 2021.
[42] J. Rodriguez, R. M. Kennel, J. R. Espinoza, M. Trincado, C. A. Silva, and C. A. Rojas, "High-performance control strategies for electrical drives: An experimental assessment," *IEEE Trans. Ind. Electron.*, vol. 59, no. 2, pp. 812–820, Feb. 2012, doi: 10.1109/TIE.2011.2158778.
[43] C. A. Rojas, J. R. Rodriguez, S. Kouro, and F. Villarroel, "Multiobjective fuzzy-decision-making predictive torque control for an induction motor drive," *IEEE Trans. Power Electron.*, vol. 32, no. 8, pp. 6245–6260, Aug. 2017, doi: 10.1109/TPEL.2016.2619378.

Taoming Wang (Student Member, IEEE) was born in Shanxi, China, in 1993. He received the B.S. degree in electrical engineering from the Shaanxi University of Technology, Hanzhong, China, in 2011, and the M.S. degree in electrical engineering from the Taiyuan University of Science and Technology, Taiyuan, China, in 2018. Since 2018, he has been working toward the Ph.D. degree in electrical engineering with Northwestern Polytechnical University, Xi'an, China.

His research interests include predictive control for power electronics and electric drives, and application of the field-programmable-gate-arrays-based digital controller.

Guangzhao Luo (Senior Member, IEEE) received the M.S. and Ph.D. degrees in electrical engineering from Northwestern Polytechnical University (NPU), Xi'an, China, in 1998 and 2003, respectively.

From 2003 to 2004, he was a Postdoctoral Research with the University of Federal Defense, Munich, Germany. He is currently a Professor with NPU. He is the Vice Director of the Rare Earth Permanent Magnet Electric Machine and Control Engineering Center, Shaanxi, China. His research interests include advance control theory of permanent-magnet electrical machine, high-performance control technology of permanent-magnet synchronous motor for electric traction and electric vehicle, real-time simulation technology for electrical drive system, and intelligence control of new energy conversion.

Dr. Luo was the recepient of the Second Prize from the China National Defense Science and Technology Progress Award in 1995 and 2011.

Zhe Chen (Member, IEEE) was born in Shanxi, China, in 1986. He received the B.S. and M.S. degrees in electrical engineering from the Automation Faculty, Northwestern Polytechnical University, Xi'an, China, in 2008 and 2011, respectively, and the Ph.D. degree in electrical engineering with the Institute for Electrical Drive Systems and Power Electronics, Technical University of Munich, Munich, Germany, in 2016.

Since 2017, he has been working as an Associate Professor with Northwestern Polytechnical University. His research interests include predictive control and sensorless control for power electronics and electric drives, renewable energy systems, and application of field-programmable-gate-arrays-based digital controllers.

Wencong Tu (Member, IEEE) was born in Shaanxi, China, in 1988. He received the B.S., M.S., and Ph.D. degrees in electrical engineering from the Automation Faculty, Northwestern Polytechnical University, Xi'an, China, in 2011, 2014, and 2019, respectively.

Since 2020, he has been an Engineer with AVIC Shaanxi Aero Electric Co., Ltd., Xi'an. His research interests include predictive control for power electronics and electric drives, real-time simulation technology for electrical drives system, and application of field-programmable-gate-arrays-based digital controllers.

Chunqiang Liu (Member, IEEE) was born in Henan, China, in 1990. He received the B.S. and M.S. degrees in electrical engineering from the Xi'an University of technology, Xi'an, China, in 2012 and 2015, respectively, and the Ph.D. degree in electrical engineering from Automation Faculty, Northwestern Polytechnical University, Xi'an, China, in 2021.

His research interests include aviation electromechanical actuation system, active disturbance rejection control for power electronics, and electric drives.